Rotational Eddy Current Speed Sensor

Mehran Mirzaei, Pavel Ripka, Jan Vyhnanek, Andrey Chirtsov, and Vaclav Grim

Faculty of Electrical Engineering, Czech Technical University, Prague, 16627, Czech Republic

A novel eddy current speed sensor is developed to measure rotational speed of conductive objects. The sensor consists of one excitation coil and two pick up coils around rotating cylinder or rod. The sensor does not use magnetic yoke. For the analysis and experimental verification we used 30 mm diameter non-magnetic aluminum and also magnetic solid iron cylinders. The calculated and measured speed range is until 1200 rpm. 2D analytical method is developed to calculate sensor performance. 2D finite element is also used for simulations to compare results with 2D analytical method. 3D finite element analysis is required to take into account significant 3D effects due to the air coils configuration. The experimental results are presented at different steady state speeds. The calculations results are compared with measurements to validate theoretical models and sensor performance. The eddy current speed sensor shows high linearity even at low speeds. For ferromagnetic rods we suggest novel double-layer configuration: non-magnetic conductive ring or shell on top of the iron rod minimizes the influence of the permeability changes. The main advantage of the novel sensor is that it has neither mechanical nor electrical contact to the rotating rod.

Index Terms—Rotational speed sensor, eddy current, 2D analytical method, 2D and 3D finite element method, air coil.

I. INTRODUCTION

THE SPEED sensors are key component of control and monitoring systems in linear and rotating machines [1]-[2]. Optical speed sensors are representatives of well-established nonmagnetic technology. Magnetic speed sensors utilize variable reluctance effect, eddy current effect and Hall effect [3]. The contactless magnetic speed sensors are better option for industrial speed sensors application in harsh environment with high probability of dirt and dust in comparison with nonmagnetic speed sensors. Existing magnetic speed sensors usually use permanent magnets or current carrying coils as excitation source. Permanent magnets are either mounted on the moving part or stationary – in both cases the sensors suffer from the temperature dependence of the magnet properties and they are also sensitive to the change in the distance between moving and stationary part [4]-[5].

Speed probe based on eddy currents and reluctance variations in metallic body moving in the field of permanent magnet using Hall sensor or pick up coil were presented for some applications in [5]-[6]. A speed sensor based on high sensitivity of an amorphous core with ring shape mounted on solid iron E shape core for magnetic field excitation was shown in [7], which has disadvantage of the necessity of using amorphous core with zero-magnetostriction and sharp rectangular *B-H* curve. Different structures of eddy current speed sensor with non-perpendicular and perpendicular coils were presented with analytical models based on Fourier transform in [8]-[10]. Speed sensor based on linear variable differential transformer (LVDT) configuration with ferrite yoke is presented in [11], which was presented for flat type moving part using outcomes of [8]-[10]. Non-ferromagnetic moving conductors such as aluminum are only used in [5]-[11], which are not complicated for measurement and simulations. An eddy current linear speed sensor with

Corresponding author: M. Mirzaei (e-mail: mirzameh@fel.cvut.cz).

axisymmetric structure was developed and measured at variable linear speeds with ferromagnetic iron rod [12], which magnetic relative permeability was measured and estimated for precise simulations and analysis. Rotational eddy current speed sensor could be very appropriate option for some applications such as turbochargers [13]-[15], which is problematic for conventional speed sensor.

In our linear speed sensor we use single coil excitation coil with AC current and two antiserially connected pick up coils for the measurement [12] without using ferromagnetic yoke as back iron for flux. In his paper we suggest similar scheme for rotational speed sensing. Despite the similar principle, the description of the rotational sensor requires different approach.

Fast and precise 2D analytical methods are presented to calculate excitation coil inductance and coupling inductances and induced voltages into the pick up coils taking into account eddy currents in the rotating conductive rod caused by alternating current and moving conductive rod speed for a rotating model using Fourier series. General closed-form equations are also obtained for output results. 2D and 3D finite element method (FEM) simulations with consideration of rotating part speed are also presented to compare with analytical calculations and consider 3D effects. Different relative magnetic permeabilities are considered for the rotating solid iron part. Cylindrical aluminum rod and solid ferromagnetic iron rod are both used in the measurement for rotating part and the experimental results are compared with the analytical and FEM calculations. The induced voltages of pick-up coils are measured with lock-in amplifier.

The main novelty of the present paper is double-layer configuration: non-magnetic conductive ring on top of the iron rod minimizes the influence of the permeability changes of the rod.

II. MODEL AND COILS CONFIGURATIONS

Fig. 1 shows 3D model of rotating rod and speed sensor

coils. The middle coil is considered as excitation coil and left and right hand sides coils are pick up coils in the first configuration. It is also possible to use left and right hand side antiserially connected coils as excitation coils and middle coil as pick up coil. Rotating rod is solid iron or aluminum. The axial length of rotating rod is considered large enough in comparison with coils dimensions.

It is clear that induced voltage in the pick up coils in both above mentioned configurations is zero at zero speed because the net flux linkage is zero.

Fig. 2 and Table I show parameters and dimensions of rotational speed sensor. Parameters r_i, r_{wi}, r_{wo}, g, θ_o, θ_i, L_i, σ_{al}, σ_i and μ_i are outer radius of rotating rod, inner radius of coils, outer radius of coils, gap between coils and rotating rod, outer angle of coils, inner angle of coils, straight part length of coils in axial z-direction, aluminum electrical conductivity, iron electrical conductivity and iron relative magnetic permeability, respectively.

TABLE I
ROTATING SPEED SENSOR PARAMETERS

Parameters	Values
I	172.36 mA
N	50
r_i	15 mm
r_{wi}	16.25mm
r_{wo}	18.25 mm
$g = r_{wi} - r_i$	1.25 mm
θ_o	46 Deg.
θ_i	33.4 Deg.
L_i	30 mm
σ_{al}	21.5 MS/m
σ_i	5.54 MS/m
μ_{ri}	100

III. 2D MODELING

A. Analytical

The Maxwell equations are used to compute speed sensor performance [16]-[17]. Final differential equations in cylindrical coordinate have only axial z-component of magnetic vector potential, A_z and current density, J_z because of 2D configuration. Magnetic flux density and magnetic field strength have only radial and azimuthal components, B_r, B_θ, H_r and H_θ, respectively:

$$
\begin{bmatrix} B_r \\ B_z \end{bmatrix} = \begin{bmatrix} \mu & 0 \\ 0 & \mu \end{bmatrix}\begin{bmatrix} H_r \\ H_z \end{bmatrix}
$$
$$
\frac{1}{r}\left(\frac{\partial(rH_\theta)}{\partial r} - \frac{\partial H_r}{\partial \theta}\right) = J_z, \frac{1}{r}\left(\frac{\partial(rB_r)}{\partial r} + \frac{\partial B_\theta}{\partial \theta}\right) = 0
$$
$$
\begin{bmatrix} \frac{1}{r}\frac{\partial J_z}{\partial \theta} \\ -\frac{\partial J_z}{\partial r} \end{bmatrix} = \begin{bmatrix} -\sigma\frac{dB_r}{dt} \\ -\sigma\frac{dB_\theta}{dt} \end{bmatrix}, \begin{bmatrix} B_r \\ B_\theta \end{bmatrix} = \begin{bmatrix} \frac{1}{r}\frac{\partial A_z}{\partial \theta} \\ -\frac{\partial A_z}{\partial r} \end{bmatrix}
$$
(1)

where, μ and σ are magnetic permeability and electrical conductivity, respectively.

The induced eddy current in the rotating rod with electrical conductivity, σ due to the iron rod speed, ω_r must be considered in the equations [18]-[19]:

$$
J_z = -\sigma\left(\frac{\partial A_z}{\partial t} + \frac{d\theta}{dt}\frac{\partial A_z}{\partial \theta}\right) = -\sigma\left(\frac{\partial A_z}{\partial t} + \omega_r\frac{\partial A_z}{\partial \theta}\right)
$$
(2)

The computational model is divided to four parts. Parts 1, 2, 3 and 4 are rotating rod region, air region between rotating rod and coils, coils region and air region beyond coils, respectively.

$$
\frac{1}{r}\frac{\partial}{\partial r}\left(r\frac{\partial A_{z,1}}{\partial r}\right) + \frac{1}{r^2}\frac{\partial^2 A_{z,1}}{\partial \theta^2} = \mu_1 \cdot \sigma\left(\frac{\partial A_{z,1}}{\partial t} + \omega_r \cdot \frac{\partial A_{z,1}}{\partial \theta}\right)
$$
(3)

$$
\frac{1}{r}\frac{\partial}{\partial r}\left(r\frac{\partial A_{z,3}}{\partial r}\right) + \frac{1}{r^2}\frac{\partial^2 A_{z,3}}{\partial \theta^2} = -\mu_3 \cdot J_s
$$
(4)

$$
\frac{1}{r}\frac{\partial}{\partial r}\left(r\frac{\partial A_{z,2,4}}{\partial r}\right) + \frac{1}{r^2}\frac{\partial^2 A_{z,2,4}}{\partial \theta^2} = 0
$$
(5)

where, J_s is the source current density in the coils.

The method of separation of variables (method of Fourier) is used to solve (3), (4) and (5) [16]-[17].

They are assumed that magnetic fields change sinusoidal versus time and periodically in θ-direction with period length 2π. Therefore derivations could be replaced as follows:
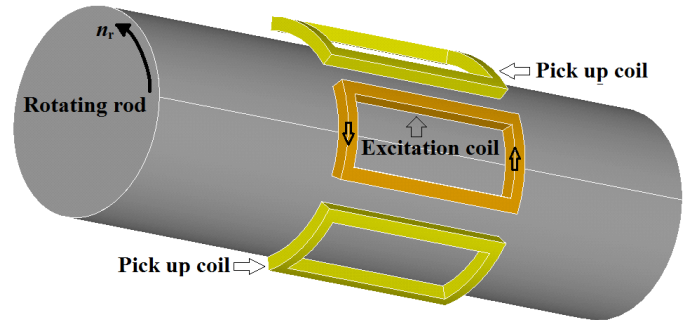

Fig. 1. 3D model of rotating eddy current speed sensor - First configuration of coils: one excitation coil and two antiserially connected pick up coils
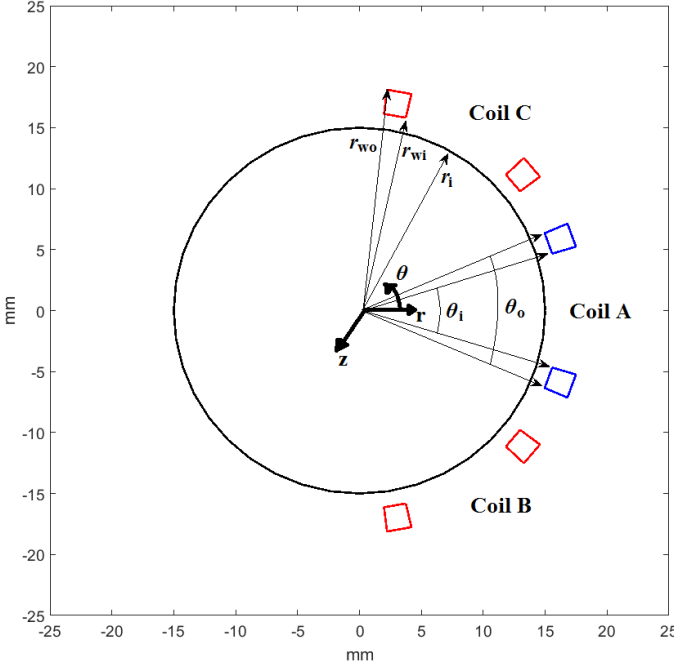
Fig. 2. 2D model and dimensions

$$A_z = \Theta(\theta) \cdot R(r) \cdot T(t) \tag{6}$$

$$
\begin{aligned}
&\Theta(\theta) \propto \exp(-jm \cdot \theta) \\
&T(t) \propto \exp(j\omega \cdot t) \\
&\frac{\partial A_z}{\partial t} = j\omega \cdot A_z \\
&\frac{\partial A_z}{\partial \theta} = -jm \cdot A_z, \quad \frac{\partial^2 A_z}{\partial \theta^2} = -m^2 \cdot A_z
\end{aligned}
\tag{7}
$$

where, ω is angular frequency in rad/s.

The solutions versus radius, r are as follows:

$$
\begin{aligned}
&A_{z,1} = \sum_{m=\pm 1,\pm 2,\ldots}\left(C_{11}\text{BesselI}(m_1,\gamma \cdot r) + C_{12}\text{BesselK}(m_1,\gamma \cdot r)\right) \\
&\gamma = \sqrt{j\mu_1\sigma(\omega - m \cdot \omega_r)} \\
&A_{z,2} = \sum_{m=\pm 1,\pm 2,\ldots}\left(C_{21}r^{m_1} + C_{22}r^{-m_1}\right) \\
&A_{z,3} = \sum_{m=\pm 1,\pm 2,\ldots}\left(C_{31}r^{m_1} + C_{32}r^{-m_1} + A_{z,s}\right) \\
&A_{z,s} = \frac{\mu_3 J_m}{m^2-4}\cdot r^2 \ (m_1 \neq 2), A_{z,s} = \frac{\mu_3 J_m}{16}\cdot r^2(1-4\log(r)) \\
&(m_1 = 2) \\
&A_{z,4} = \sum_{m=\pm 1,\pm 2,\ldots}\left(C_{41}r^{m_1} + C_{42}r^{-m_1}\right) \\
&m_1 = |m|
\end{aligned}
\tag{8}
$$

where, C_{11}, C_{12}, C_{21}, C_{22}, C_{31}, C_{32}, C_{41} and C_{42} are constants and they are obtained by the following boundary conditions:

$$
\begin{aligned}
&A_{z,1}(r=0) = 0 \\
&A_{z,1}(r=r_i) = A_{z,2}(r=r_i), \ H_{\theta,1}(r=r_i) = H_{\theta,2}(r=r_i) \\
&A_{z,2}(r=r_{wi}) = A_{z,3}(r=r_{wi}), H_{\theta,2}(r=r_{wi}) = H_{\theta,3}(r=r_{wi}) \\
&A_{z,3}(r=r_{wo}) = A_{z,4}(r=r_{wo}), H_{\theta,3}(r=r_{wo}) = H_{\theta,4}(r=r_{wo}) \\
&A_{z,3}(r=\infty) = 0
\end{aligned}
\tag{9}
$$

Parameter, J_m in (8) for coils region for single coil excitation and two antiserially connected coils could be calculated as follows, respectively:

$$
\begin{aligned}
&J_m = \frac{j}{m\pi}C_J \cdot J_s \\
&J_m = \frac{-1}{m\pi}C_J \cdot J_s \cdot 2 \cdot \sin\left(\frac{m\theta_d}{2}\right) \\
&C_J = \left(\cos\left(m\frac{\theta_i}{2}\right) - \cos\left(m\frac{\theta_o}{2}\right)\right), \theta_d = \frac{2\pi}{3} \\
&J_s = \frac{NI}{\frac{(\theta_o - \theta_i)}{4}\cdot\left(r_{wo}^2 - r_{wi}^2\right)}
\end{aligned}
\tag{10}
$$

where, N and I are the number of turns per coil and current amplitude (Table I), respectively. The parameter θ_d is the angle between coils B and C centers, which is considered equal to 120 Deg. It is considered that all coils have same dimensions in this paper. Mutual induced voltage, V_M and mutual inductance, L_M could be calculated as follows [18]:

$$V_M = -\frac{d\Psi_M}{dt} = -j\omega N\oint A_z dl = -j\omega N \cdot L_i \cdot \left(A_z^+ - A_z^-\right) \tag{11}$$

$$
\begin{aligned}
&L_M = \frac{\Psi_M}{I} = \frac{N \cdot L_i \cdot \int\left(A_z^+ - A_z^-\right) \cdot ds}{I \cdot a_w} \\
&a_w = \frac{(\theta_o - \theta_i)}{4}\cdot\left(r_{wo}^2 - r_{wi}^2\right), \ ds = r \cdot dr \cdot d\theta
\end{aligned}
\tag{12}
$$

where, Ψ_M is the total average mutual flux linkage over coils 2D cross section area. The surface integration in (12) is applied on each coil cross section area. A_z^+ and A_z^- are magnetic vector potentials in go and return paths of coil. Integration in (11) is for the ideal case with infinitesimal coil cross section. Integration in (12) is for the real case of coil cross section, which is averaged over coil cross section.

The differential voltage between left and right sides pick up coils (B and C in Fig. 2) is presented in (13) and (14). The differential voltage polarity changes as speed direction changes according to (13) and (14).

$$V_d = V_{M,l} - V_{M,r} = j\omega \cdot \left(L_{M,l} - L_{M,r}\right) \cdot I \tag{13}$$

$$V_d = V_{M\,l} - V_{M\,r} = j\omega N \cdot \sum_{m=\pm 1, \pm 2,\ldots} \left(C_V C_J \frac{4}{m} \sin\left(\frac{m\theta_d}{2}\right) \right)$$

$$C_V = C_{31} \frac{r_{wo}^{m_1+2} - r_{wi}^{m_1+2}}{m_1+2} + C_{32} \frac{r_{wo}^{-m_1+2} - r_{wi}^{-m_1+2}}{-m_1+2} + \frac{\mu_3 J_m}{m^2-4} C$$

$$C = \frac{r_{wo}^4 - r_{wi}^4}{4} \quad (m_1 \neq 2),$$

(14)

$$C_V = C_{31} \frac{r_{wo}^{m_1+2} - r_{wi}^{m_1+2}}{m_1+2} + C_{32} \log\left(\frac{r_{wo}}{r_{wi}}\right) + \frac{\mu_3 J_m}{16} C$$

$$C = \frac{r_{wo}^4 - r_{wi}^4}{4} -$$

$$\left(r_{wo}^4 \cdot \left(\log(r_{wo}) - \frac{1}{4} \right) - r_{wi}^4 \cdot \left(\log(r_{wi}) - \frac{1}{4} \right) \right) \quad (m_1 = 2)$$

Magnetic flux penetration in the rotating rod decreases with AC excitation current [19] at 30 Hz and 90 Hz and +1200 rpm speed due to the skin effect (Fig. 3- Fig. 4). Less flux penetration in the rotating rod at higher frequency causes less differential mutual flux linkage and decreases speed sensitivity of the eddy current speed sensor (Table. II).

TABLE II
DIFFERENTIAL MUTUAL FLUX LINKAGE AT DIFFERENT FREQUENCIES -
+1200 RPM

Frequency (Hz)	Flux linkage amplitude (µVs)- Iron / Aluminum
20	0.92 / 1.73
50	0.30 / 1.62
100	0.20 / 1.32
500	0.07 / 0.25
1000	0.04 / 0.10

B. FEM

2D time transient finite element with consideration of motion is considered for numerical calculations [20]. Fig. 5 shows differential voltage amplitude results of antiserially connected pick up coils versus speed using 2D analytical and 2D FEM. The analytical calculations coincide well with 2D FEM, which shows accuracy of analytical method. Excellent linearity is depicted in Fig. 5, which presents suitability of proposed sensor for speed measurement. Higher frequency 90 Hz is more suitable for differential voltage measurement despite lower flux linkage at higher frequencies.
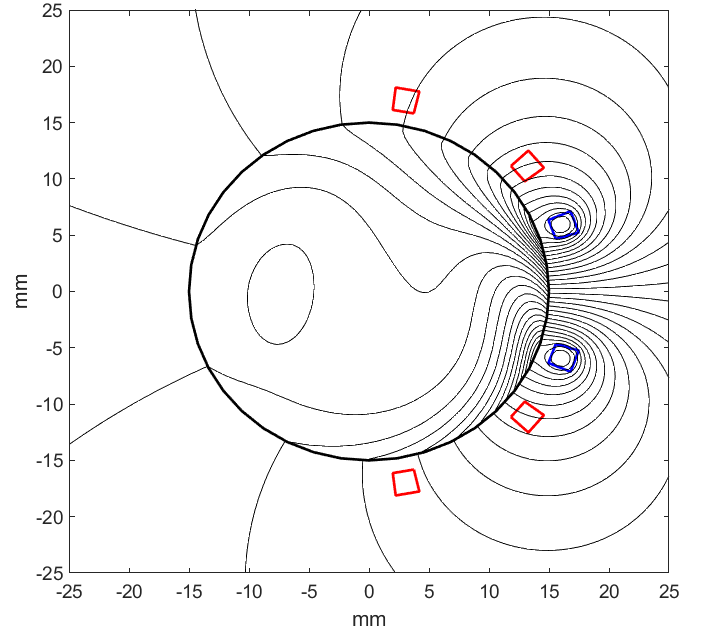

Fig. 3. Magnetic flux distribution at 30 Hz and +1200 rpm with rotating iron rod - First configuration of coils: one excitation coil and two antiserially connected pick up coils - Analytical method
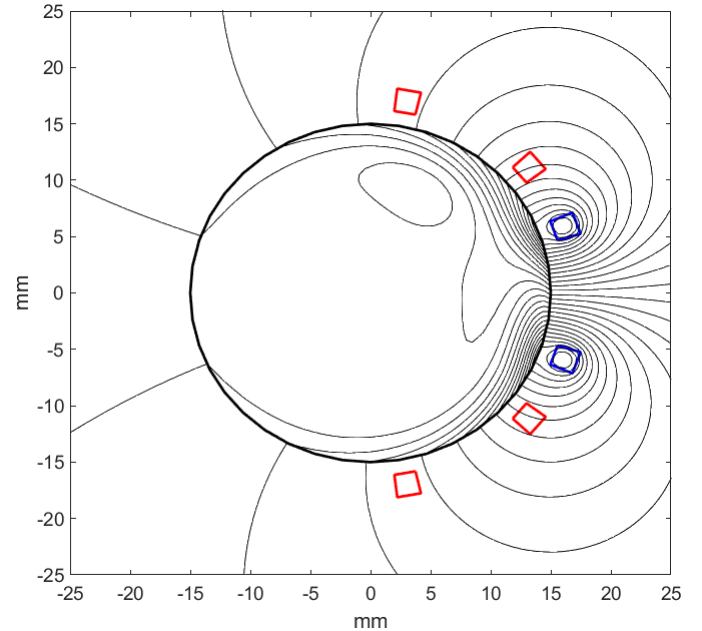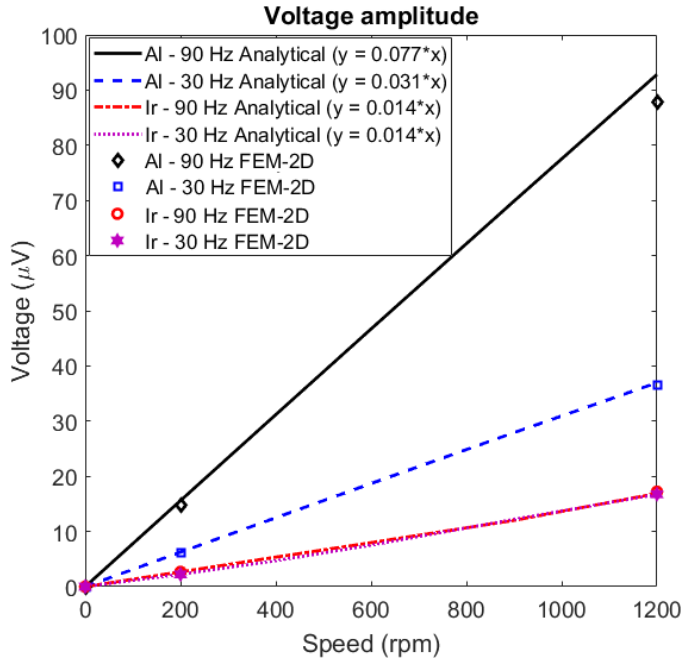

Fig. 4. Magnetic flux distribution at 90 Hz and +1200 rpm with rotating iron rod - First configuration of coils: one excitation coil and two antiserially connected pick up coils - Analytical method

Fig. 5. Induced voltage versus speed for rotating aluminum rod (Al) and rotating iron rod (Ir) - Analytical versus 2D FEM

C. Parameters variation

Fig. 6 shows changing of magnetic flux distribution for rotating iron rod at +1200 rpm and 90 Hz and flux linkage between pick up coils and excitation coil with decreasing gap, g (left) and increasing gap and coils angles, θ_o and θ_i (right). The difference between outer angle and inner angles of coils are considered constant in this paper. 3D graphs in Fig. 7 - Fig. 8 related to variations of differential induced voltage amplitude versus gap and outer angle of coils, show several tendencies. Increasing outer angle of coils to maximum value, 60 Deg. increases coupling between excitation coil and pick up coils and differential induced voltage.

Decreasing gap does not have the same effect for the iron and aluminum rods as the flux leakage (non-coupled flux between the excitation coil and the pick up coils) increases with decreasing gap below 2 mm due to the high magnetic permeability of iron in comparison with aluminum. The maximum values of differential induced voltages are 30 µV for rotating iron rod and 145 µV for aluminum rod, respectively. Optimum and efficient gap for rotating iron rod for maximum differential voltage is calculated 1.75-2 mm with outer angle of coils 60 Deg. (Fig. 7). Larger airgap is mechanically better and coils are safer when rod is rotating at high speeds. Fig. 9 presents differential induced voltage versus relative permeability and conductivity for rotating iron rod. Decreasing magnetic relative permeability causes higher induced voltage similar to increasing iron electrical conductivity. It also shows that relative magnetic permeability has higher influence than electrical conductivity. This is a weak point of such sensor, as permeability is temperature dependent. The differential induced voltage versus electrical conductivity for nonmagnetic rotating rod ($\mu_r = 1$) is shown in

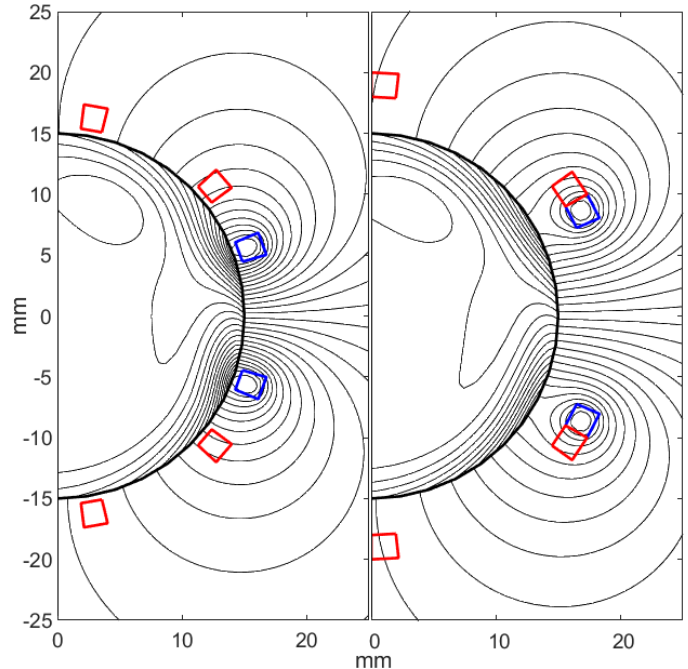Fig. 10. It can be concluded, for example, copper is more efficient than aluminum.

Fig. 6. Magnetic flux distribution at 90 Hz and +1200 rpm with rotating iron rod –(left) modified gap between coils and rod, g to 0.5 mm (r_{wi}-r_i = 0.5 mm) and (right) modified gap, g to 3 mm and also modified coil inner angle, θ_i = 47.4 Deg. and modified coil outer angle θ_o = 60 Deg. - Analytical method
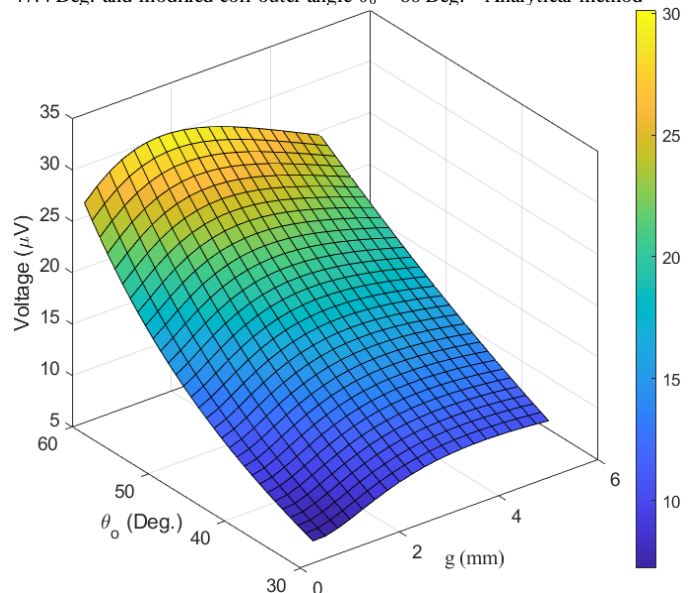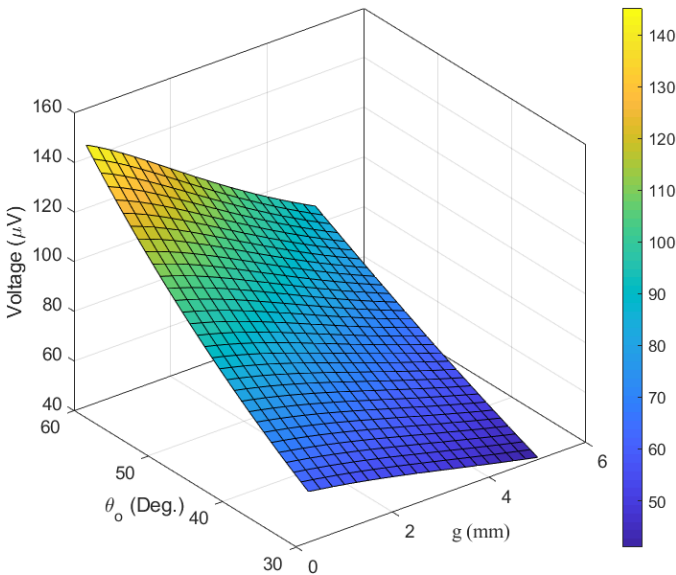

Fig. 7. Variation of differential voltage (amplitude) versus gap, g and outer angle of coil, θ_o for rotating iron rod at 90 Hz and 1200 rpm - Analytical method

Increasing frequency until 1000 Hz increases differential induced voltages for aluminum and iron rods as shown in Fig. 11. The curves for rotating iron rod and aluminum rods do not have same tendency versus frequency because of high permeability of iron rod. Very high frequency is not recommended because the surface properties of conductive rods have large influence due to small penetration depth. The surfaces of conductive objects are usually more affected, for

example, by manufacturing process and corrosion.

Skin depths are presented in Table. III at different frequencies. Larger skin depths cause larger differential flux linkage as shown in Table II and larger differential voltage.

Only linear magnetic modeling using initial permeability is considered in this paper due to the low magnetic fields in the sensor and nonlinearity and hysteresis effects are neglected. Relative magnetic permeability, $\mu_{ri} = 100$ (Table. I) is selected for the used rotating iron rod in this paper.

TABLE III
SKIN DEPTH AT DIFFERENT FREQUENCIES

Frequency (Hz)	Skin depth, δ (mm)- Iron / Aluminum
20	4.8 / 24.3
50	3.0 / 15.4
100	2.1 / 10.9
500	1.0 / 4.9
1000	0.7 / 3.4
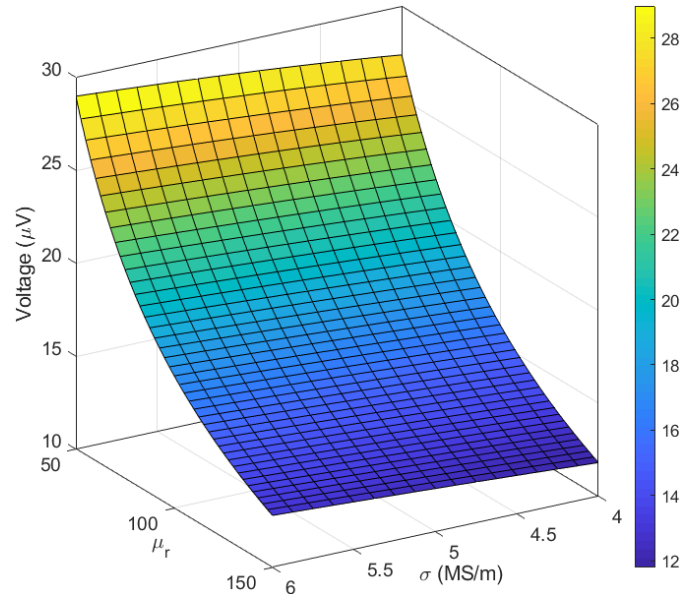
Fig. 9. Variation of differential voltage (amplitude) versus electrical conductivity and magnetic permeability for rotating iron rod at 90 Hz and 1200 rpm (θ_o = 46 Deg. and g = 1.25 mm) - Analytical method

Fig. 8. Variation of differential voltage (amplitude) versus gap, g and outer angle of coil, θ_o for rotating aluminum rod at 90 Hz and 1200 rpm - Analytical method
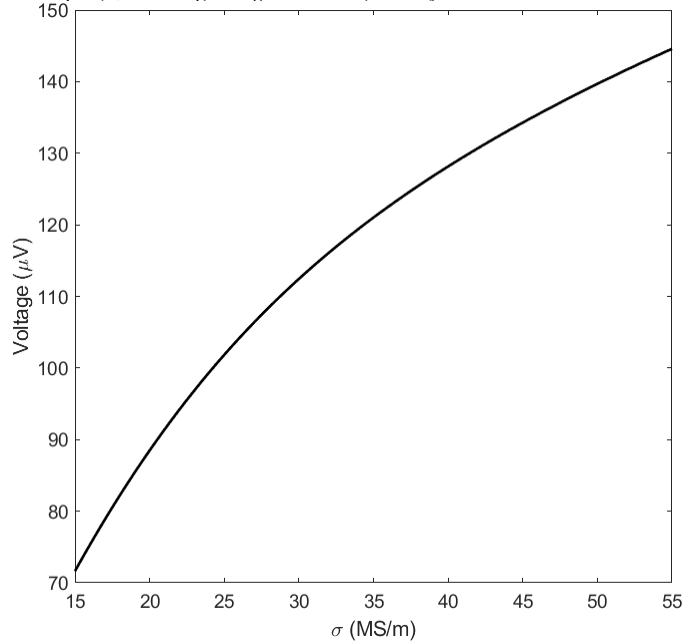

Fig. 10. Variation of differential voltage (amplitude) versus electrical conductivity for rotating aluminum rod at 90 Hz and 1200 rpm (θ_o = 46 Deg. and g = 1.25 mm) - Analytical method
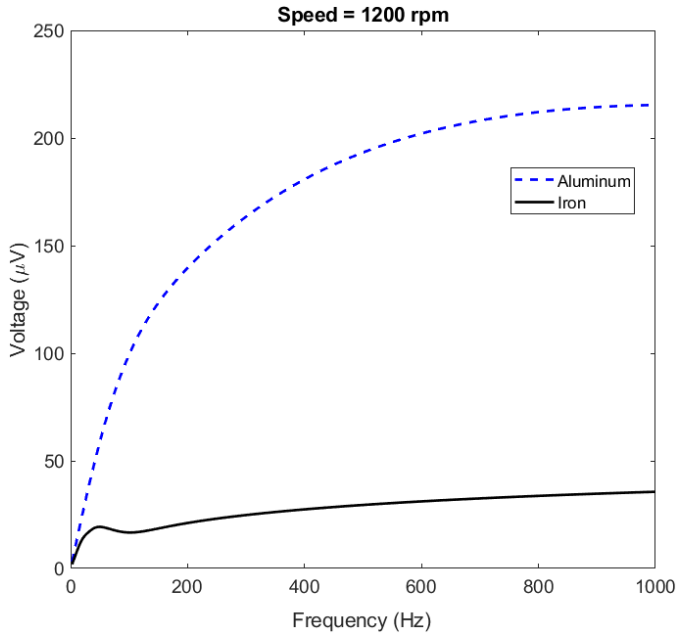
Fig. 11. Variation of differential voltage (amplitude) versus frequency at 1200 rpm (θ_o = 46 Deg. and g = 1.25 mm) - Analytical method

IV. 3D FEM MODELING

A. Static rotor

3D analysis is required for more accurate analysis of air coils eddy current speed sensor to take into account 3D effects such as 3D flux and eddy currents distributions in the conductive rotating rods. First 3D eddy current analysis (time harmonic) was done using Ansys/Maxwell software package [20] to evaluate 3D FEM model accuracy and parameters such as relative permeability of iron rod as mentioned in Table I. Calculated self inductances of excitation coil and induced voltages in one of the pick up coils at different frequencies are compared with experimental results in Tables VI and V. The calculated self inductances show high accuracy. Lower accuracy in the calculated mutual induced voltage is due to the higher sensitivity to pick up coils relative locations to excitation coil and also probably manufacturing tolerance.

TABLE IV
INDUCTANCE OF EXCITATION COIL AT DIFFERENT FREQUENCIES -
3D FEM VS. EXP

Frequency (Hz)	Inductance (µH) - 3D FEM / Exp.
20 (iron core)	137.2 / 135.0
50 (iron core)	136.6 / 134.2
100 (iron core)	135.8 / 132.4
100 (air core)	98.9 / 95.0
500 (iron core)	132.4 / 129.5
1000 (iron core)	130.5 / 127.0

TABLE V
INDUCED VOLTAGES IN ONE OF PICK UP COIL AT DIFFERENT FREQUENCIES -
3D FEM VS. EXP

Frequency (Hz)	Induced voltage (mV) - 3D FEM / Exp.
1 (iron core)	0.0084 / 0.0076

100 (iron core)	0.91 / 0.85
100 (air core)	0.76 / 0.72
200 (iron core)	1.86 / 1.76

B. Rotating rotor

3D time transient FEM is used to take into account rod rotating motion [20]. Fig. 12 shows meshed model of conducting rods and coils. Half of the model is shown because of symmetry. Second orders elements are used. The sizes of elements are selected based on compromise between skin depth in the rotating rod and precise differential voltage calculations and also simulation time. The total axial length of rotating iron rod and rotating aluminum rod is considered 100 mm in the 3D FEM simulations.

V. EXPERIMENTS

Experimental set up are shown in Fig. 13 and Fig. 14. Lock-in amplifier SR 830 is used to measure precisely small voltage of pick up coils and to minimize noise effects. Signal generator with internal resistance 50 Ω is connected to the excitation coil. The aluminum or iron rod is connected to the shaft of DC motor. The speed range is between 0 to 1200 rpm. The axial length of rotating rods is considered 200 mm and 100 mm to evaluate its influence on the speed sensor performance.

Fig. 15 shows experimental results and 3D FEM calculations for differential induced voltage versus speed. The 3D FEM calculations coincide very well with experiments with small error (Fig. 16). Sensitivity of speed sensor is higher for rotating aluminum rod rather than iron rod. The linearity of eddy current speed sensor is excellent despite of simple structure of the proposed sensor. It has been verified that differential induced voltage are the same for two axial lengths of rotating rods, 100 mm and 200 mm.

The differential induced voltages are measured and calculated in 2D and 3D at 30 Hz and 90 Hz. The 3D FEM results are higher than 2D analytical and 2D FEM calculations (Fig. 5) due to the 3D effects in rotating iron rod. 3D FEM is more precise in comparison with measurement despite its longer simulations time. 3D modeling is necessary for air coil or yokeless magnetic devices. Time consuming 3D FEM models simulations slow down fast optimization and analysis, that is why 2D models, especially analytical, are preferable at design stage. Dynamic response of the eddy current speed sensor is higher at 90 Hz, which is important for acceleration and deceleration operations. The sensitivity of eddy current speed sensor for iron rod should be improved as most industrial applications are made with solid iron rather than non-magnetic stainless steel or aluminum.
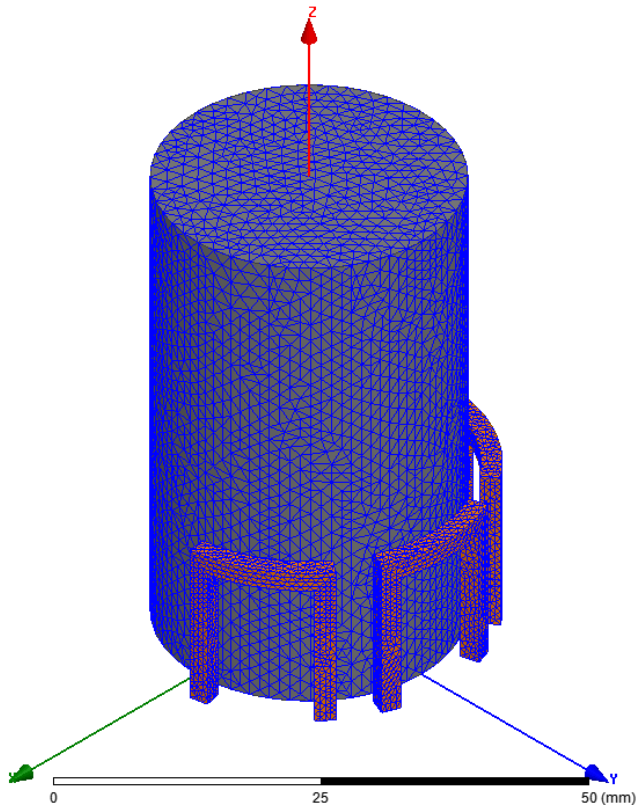
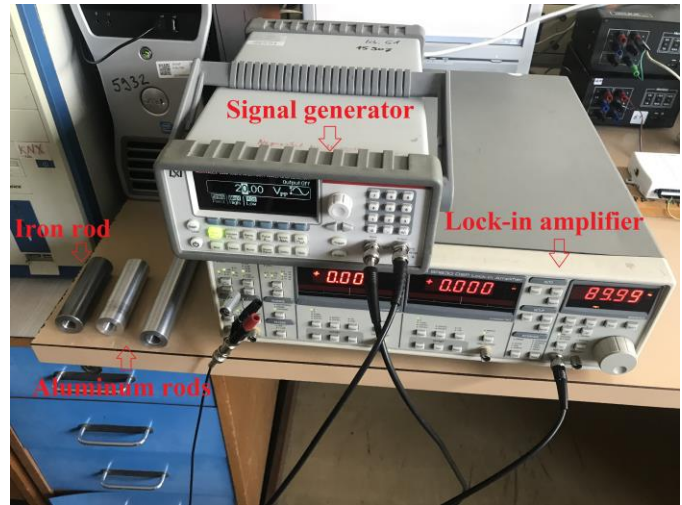Fig. 12. Meshed model of eddy current speed sensor

Fig. 13. Experimental set up for rotational eddy current speed sensor – sensor mounted on rotating rod

Fig. 14. Experimental set up for rotational eddy current speed sensor – signal generator and lock-in amplifier
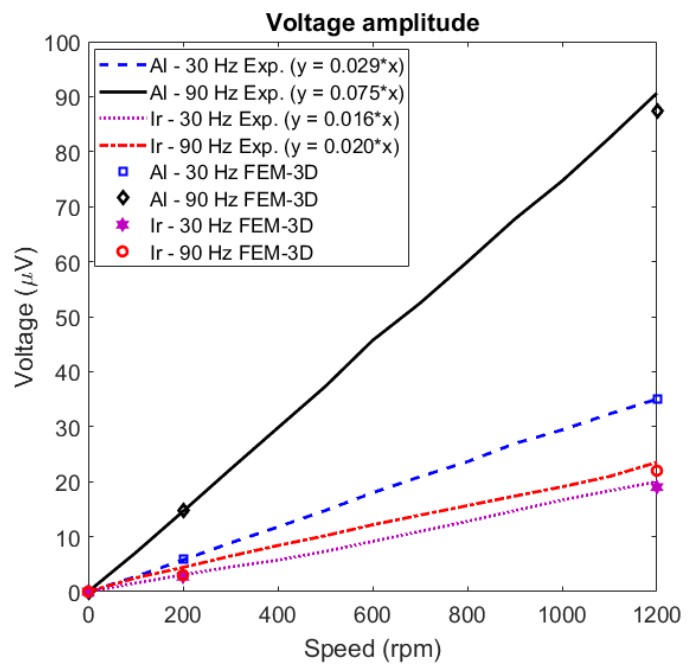

Fig. 15. Induced voltage versus speed for rotating aluminum rod (Al) and rotating iron rod (Ir) – Experiments versus 3D FEM
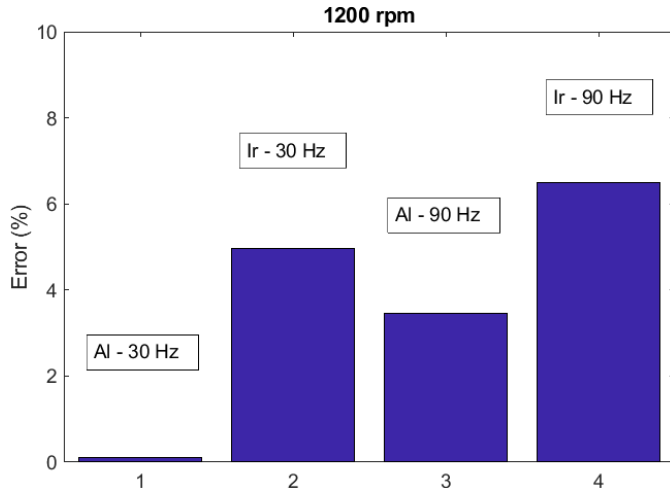
Fig. 16. Error of 3D FEM results relative to measurements

VI. DOUBLE LAYER ROD

Fig. 17 and Fig. 18 show new proposed double layer rod with magnetic flux distribution. Center rod is solid iron and aluminum shell is the second layer. Second layer could be any other nonmagnetic metal such as copper or brass. Double layer moving or rotating part is well known configuration to improve performance of solid rotor rotating induction motor or solid secondary linear induction motors [21]-[22]. It increases equivalent conductivity of rotating rod and causes low magnetic reluctance using high permeability iron part. Double layer rotating rod can be easily manufactured by adding a simple shell or ring to the iron rod.

Rotating rod in Fig. 17 has total outer radius 15 mm with iron rod radius 13 mm. Iron rod radius is considered fixed, 15 mm and total outer radius is 16 mm in Fig. 18 with 1.25 mm gap and same coils angle as Fig. 18. Both models show improved flux linkages of the pick up coils in comparison with complete iron rod.

Differential voltage variations versus aluminum shell thickness for fixed rotating rod outer radius 15 mm is shown in Fig. 19 at 90 Hz and 1200 rpm, which has maximum value, 189 µV with aluminum shell thickness 3.5 mm. It shows considerable improvement in the speed sensor output and sensitivity. The 3D and 2D FEM results approve analytical estimation for the speed sensor performance improvement with double layer configuration.

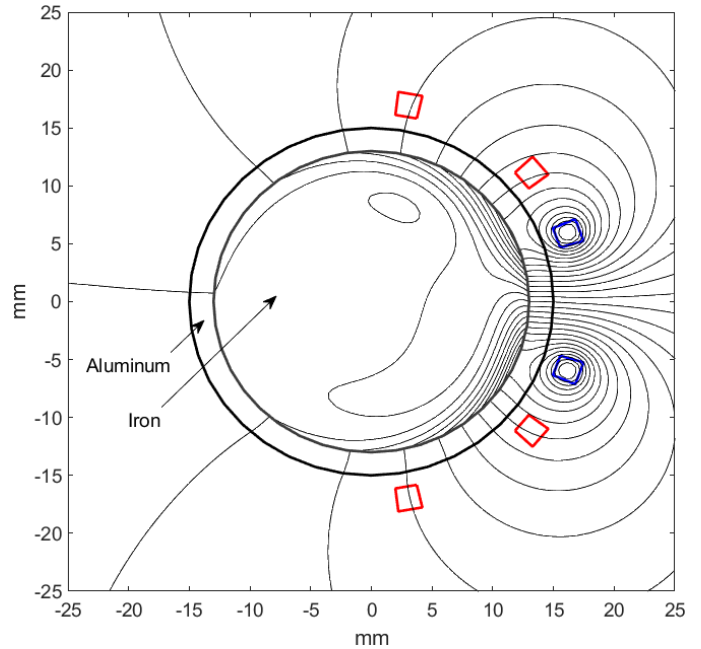Using higher conductivity aluminum shell or copper shell could increase the output differential voltage.

Fig. 17. Magnetic flux distribution at 90 Hz and +1200 rpm with double layer rotating iron (outer radius 13 mm) and aluminum shell (with 2 mm thickness) - First configuration of coils: one excitation coil and two antiserially connected pick up coils - Analytical method
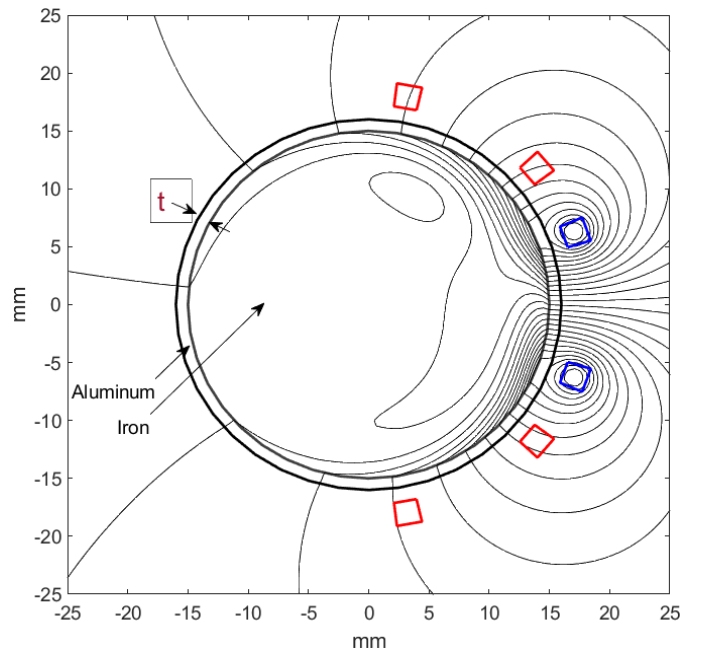

Fig. 18. Magnetic flux distribution at 90 Hz and +1200 rpm with double layer rotating iron (with radius 15 mm) and aluminum shell (with 1 mm thickness) - First configuration of coils: one excitation coil and two antiserially connected pick up coils - Analytical method
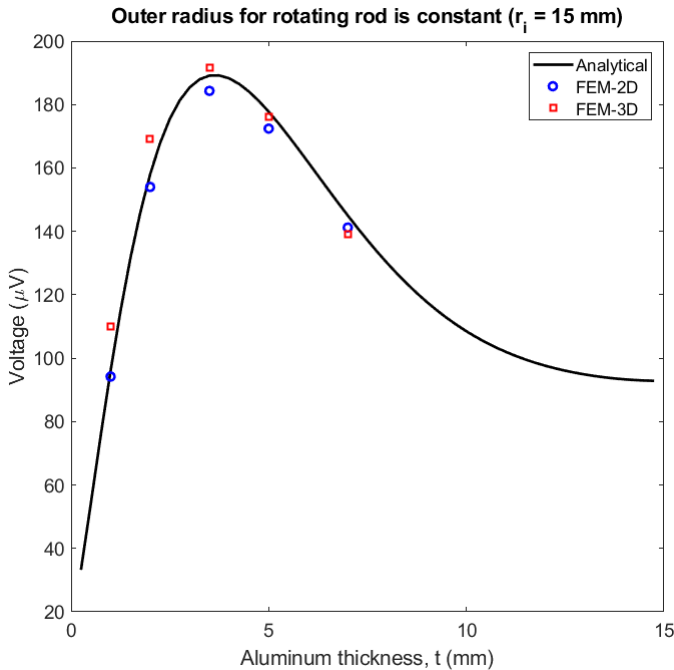
Fig. 19. Variation of differential voltage (amplitude) versus aluminum layer thickness with double layer rotating iron and aluminum shell (with t mm thickness as shown in Fig. 18) – fixed total outer radius 15 mm

Fig. 20 shows speed sensor output voltage for double layer rotating rod with fixed rotating iron rod radius, 15 mm in comparison with completely aluminum rod and iron rod with same outer radius at 90 Hz and 1200 rpm. The maximum value for induced voltage is 268 µV with aluminum shell thickness 6 mm in Fig. 20. The induced voltage in double layer rod is considerably higher than completely aluminum rod. The induced voltage in completely iron rod does not considerably increase even with much higher radius as shown in Fig. 20.
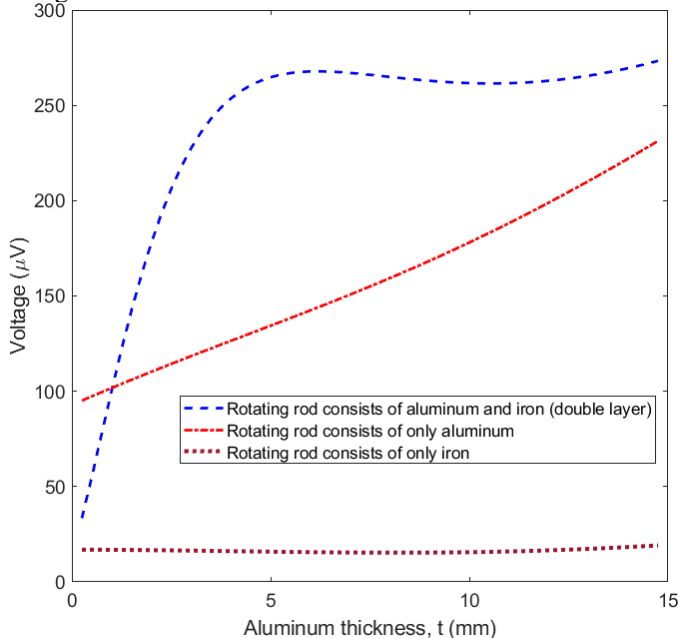
Fig. 20. Variation of differential voltage (amplitude) versus second layer shell thickness (with t mm thickness as shown in Fig. 19) – iron rod part has 15 mm radius - Analytical method

The effect of aluminum shell or ring height is evaluated in Fig. 21 and Fig. 22. Fig. 21 shows eddy current distribution for long shell and Fig. 22 shows eddy current distribution for short shell. The calculated differential induced voltage is 110 µV in long shell aluminum model and it becomes 66 µV in short shell aluminum model due to the modified path for induced eddy currents [23]-[24].

Fig. 23 presents induced voltage versus relative magnetic permeability, μ_r for different aluminum shell thickness of double layer rotating rod with fixed outer radius 15 mm at 90 Hz and 1200 rpm. Induced voltages decrease 56% for full iron rotating rod with zero aluminum shell thickness and 6.1% with 1 mm aluminum shell thickness when μ_r changes from 50 to 150. But Induced voltages only increase 0.23% with 2.35 mm aluminum shell thickness and 1.23% with 3.5 mm aluminum shell thickness. It shows that effect of relative magnetic permeability could be minimized by adjusting aluminum shell thickness. Gradient of induced voltage versus relative magnetic permeability is negative at small aluminum shell thickness and it is positive at bigger aluminum shell thickness.

The voltages are rather low, but for only 50-turn coil. Real number of turns can be higher, it is practically limited only by parasitic capacitances. For example, setting number of turns for excitation coil and pick up coils equal to 1000-turn can increase eddy current speed sensor output with gain of 2500 for the same excitation current, as the induced voltage is proportional to the square of number of turns.
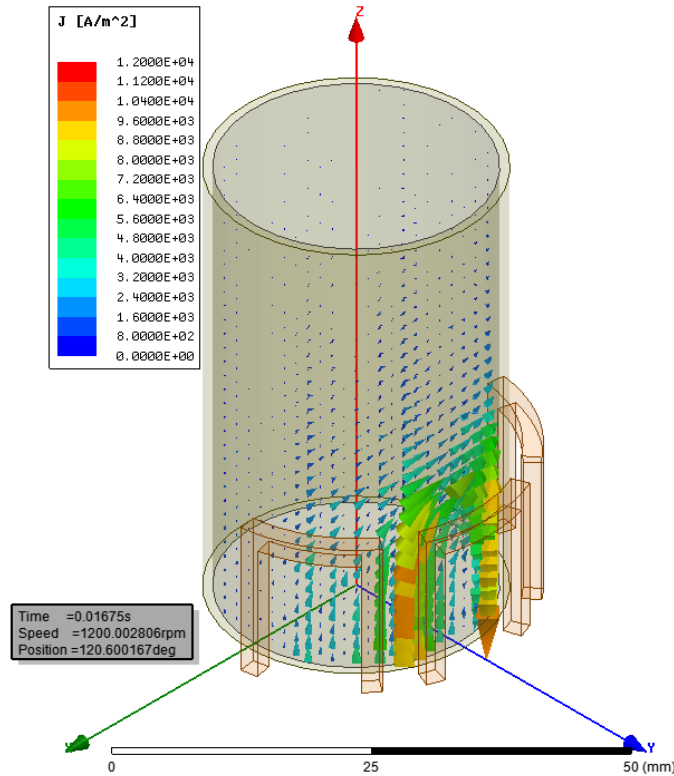
Fig. 21. Eddy currents distribution in the doubly layer rotating iron + aluminum shell at 1200 rpm and 90 Hz (outer radius of iron is 14 mm and aluminum shell thickness is 1 mm) - long aluminum shell
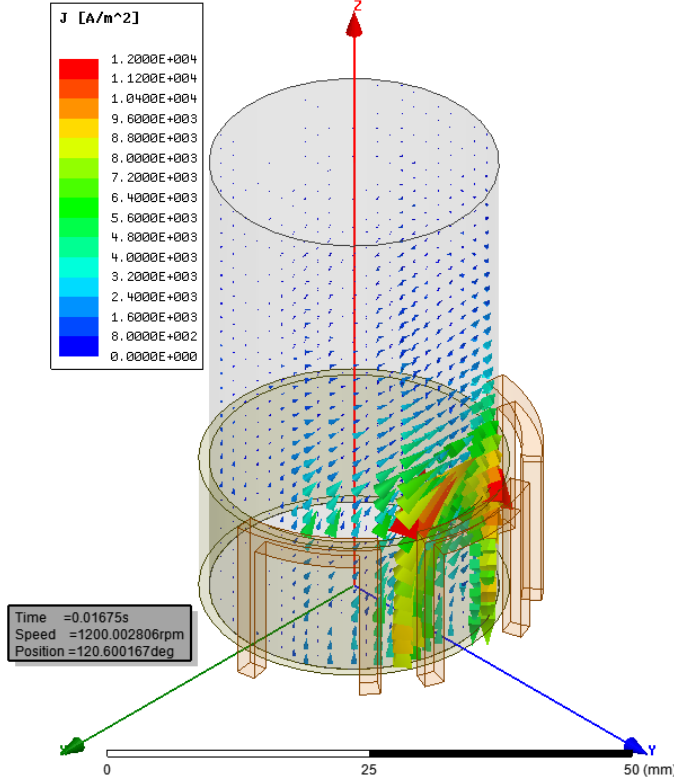

Fig. 22. Eddy currents distribution in the doubly layer rotating iron + aluminum shell at 1200 rpm and 90 Hz (outer radius of iron is 14 mm and aluminum shell thickness is 1 mm) - short aluminum shell with 30 mm height
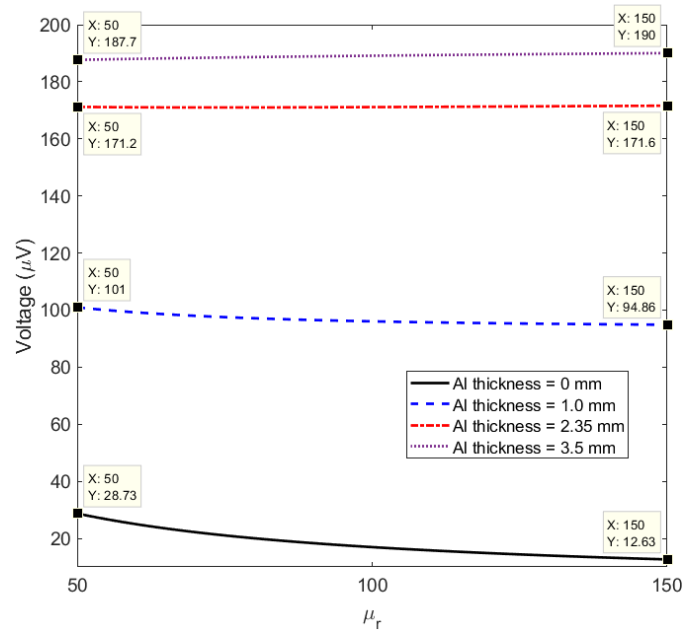

Fig. 23. Variation of differential voltage (amplitude) versus iron rod permeability at different aluminum layer thickness - 1200 rpm and 90 Hz - Analytical method

VII. CONCLUSION

A novel rotational eddy current speed sensor was presented. Analytical and numerical FEM calculations were used to analyze and improve the performance of proposed speed sensor. 2D analytical method is faster and more suitable for the design of eddy current speed sensor despite it is less precise in comparison with 3D FEM for air coil configuration.

Different configurations of rotational speed sensor and parameters were evaluated in this paper. The measurements and calculations have been done until 1200 rpm but the proposed speed sensor is also suitable for higher speeds as it does not have mechanical and electrical limitations. The whole coils span is less than 180 Deg., which could be installed in one side of rotating rod and it is mechanically contactless with rotating rod.

The double layer rod can significantly improve eddy current speed sensor performance when the rotating rod must be from magnetic steel. It needs only high electrical conductivity non-magnetic ring or shell, for example made of aluminum or copper. By using the highly conductive non-magnetic shell the sensitivity is improved and it becomes less susceptible to permeability changes.

REFERENCES

[1]   T. Addabbo, M. Di Marco, A. Fort, E. Landi, M. Mugnaini, V. Vignoli, and G. Ferretti, "Instantaneous rotation speed measurement system based on variable reluctance sensors for torsional vibration monitoring," *IEEE Trans. Ins. and Meas.*, (Early Access), pp. 1 – 11, Nov. 2018

[2]   N. Fernando, P. Arumugam, and C. Gerada, "Design of a stator for a high-speed turbo-generator with fixed permanent magnet rotor radius and volt–ampere constraints," *IEEE Trans. Energy Conv.*, vol. 33 , no. 3, pp. 1311 - 1320, Sep. 2018

[3]   P. Ripka, *Magnetic Sensors and Magnetometers*, Artech House, Jan 1, 2001 - Technology & Engineering

[4]   J. J. Costello, and A. C. Pickard, "A novel speed measurement system for turbomachinery," *IEEE Sensors Letters*, vol. 2 , no. 4, 2018

[5]   E. Cardelli, A. Faba, and F. Tissi, "Contact-less speed probe based on eddy currents," *IEEE Trans. Mag.*, 2013, vol. 49 , no. 7, pp. 3897 – 3900

[6]   T. J. Rocha, H. G. Ramos, A. L. Ribeiro, and D. J. Pasadas, "Evaluation of subsurface defects using diffusion of motion-induced eddy currents," *IEEE Trans. Instr. and Meas.*, vol. 65, no. 5, pp. 1182 - 1187, Dec. 2016

[7]   T. Sonoda, R. Ueda, K. Fujitani, T. Irisa, and S. Tatata, "DC magnetic field type eddy current speed sensor detecting cross magnetization field with amorphous core," *IEEE Trans. Mag.*, vol. 21, no. 5, pp. 1732 - 1734, Sep. 1985

[8]   N. Takehira, and A. Tanaka, "Analysis of a perpendicular-type eddy-current speed meter," *IEE Proc. A – Phys. Science, Meas. and Instr., Manag. and Educ.- Rev.* , vol. 135 , no. 2, pp. 89 - 94, Feb. 1988

[9]   T. Itaya, K. Ishida, A. Tanaka, N. Takehira, and T. Miki, "Eddy current distribution for a rectangular coil arranged parallel to a moving conductor slab," *IET Science, Meas. & Tech.*, vol. 6, no. 2, pp. 43 - 51, Mar. 2012

[10] T. Itaya, K. Ishida, A. Tanaka, and N. Takehira, "Analysis of a fork-shaped rectangular coil facing moving sheet conductors," *IET Science, Meas. & Tech.* , vol. 3 , no. 4, pp. 279 - 285, Jul. 2009

[11] A. Tuysuz, M. Flankl, J. W. Kolar, and A. Mutze, "Eddy-current-based contactless speed sensing of conductive surfaces," *IEEE 2nd Annual Southern Power Electronics Conference (SPEC)*, pp. 1 - 6, Dec. 2016

[12] M. Mirzaei, P. Ripka, A. Chirtsov, and J. Vyhnanek, "Eddy current linear speed sensor," *IEEE Trans. Mag.*, vol. 55 , no. 1 , pp. 1-4, Jan. 2018

[13] J. Rickman, "Eddy current turbocharger blade speed detection," *IEEE Trans. Mag.*, vol. 18 , no. 5, pp. 1014 - 1021, Sep. 1982

[14] D. Gerada, X. Huang, C. Zhang, H. Zhang, X. Zhang, and C. Gerada, "Electrical machines for automotive electrically assisted turbocharging ," *IEEE/ASME Trans. Mech.*, vol. 23 , no. 5, pp. 2054 – 2065, June 2018

[15] M.-S. Lim, J-M Kim, Y-S. Hwang, J-P Hong, "Design of an ultra-high-speed permanent-magnet motor for an electric turbocharger considering speed response characteristics," *IEEE/ASME Trans. Mech.*, vol. 22, no. 2 , pp. 774 - 784, Dec. 2017

[16] K.J. Binns, P.J. Lawrenson, and C.W. Trowbridge, *The Analytical and Numerical Solutions of Electric and Magnetic Fields*, Published by John Wiley & Sons Ltd., 1992

[17] M. N. O. Sadiku, *Numerical Techniques in Electromagnetics*, Second Edition, July 12, 2000 by CRC Press, Textbook

[18] K. Davey, "Analytic analysis of single- and three-phase induction motors," *IEEE Trans. on Mag.*, vol. 34, no.5, pp. 3721- 3727, Sept. 1998

[19] D. Schieber, *Electromagnetic Induction Phenomena*, Springer-Verlag, 1986 - Science

[20] Ansys-Maxwellsoftware, Accessed on 23.01.2019:https://www.ansys.com/products/electronics/ansys-maxwell

[21] S.A. Nasar, L. D. Cid, "Certain approaches to the analysis of single-sided linear induction motors," *Proc. of the Inst. of Elect. Eng.*, vol. 120 , no. 4, pp. 477 – 483, April 1973

[22] J. F. Gieras, and J. Saari, "Performance calculation for a high-speed solid-rotor induction motor," *IEEE Trans. Indus. Elect.*, vol. 59 , no. 6, pp. 2689 - 2700, June 2012

[23] H. Bolton, "Transverse edge effect in sheet-rotor induction motors," *Proc. of the Inst. of Elect. Eng.*, vol. 116, no. 5, pp. 725 - 731, May 1969

[24] H. Seo, J. Lim, G. Choe. J. Choi, and J. Jeong, "Algorithm of linear induction motor control for low normal force of magnetic levitation train propulsion system, " *IEEE Trans. on Mag.* , vol. 54, no. 11, pp. 1-4, Jul. 2018,